Characterizing Optical Transmission Through Sessile Water Droplets Undergoing Solidification

Sandeepan Dasgupta[1] and Kishan Bellur [*1]

[1]Mechanical and Materials Engineering, University of Cincinnati, Cincinnati, OH,45220

August 20, 2024

Abstract

The current increase in the usage of solar panels in cold weather climates requires a comprehensive understanding of droplet freezing. Freezing dynamics of a water droplet resting on a hydrophobic surface is well understood but changes in optical transmission during this process have not received much attention. As the droplet freezes, its refractive index and the shape change simultaneously. Here, an attempt is made to characterize the change in optical transmission during the freeing process using a unique setup that allows for bidirectional imaging of a droplet as it undergoes freezing on coated glass slides. This allows for phase change dynamics to be decoupled from the change in droplet geometry. There is a 45% reduction in optical transmission during the freezing process, but this is primarily due to reflection and not attenuation. The droplet geometry is observed to influence a change in optical transmission due to changes in both reflection and attenuation. Common hydrophobic coatings are tested and their influence on the optical transmission is characterized. The results of this study provides new insight in the development of optically transparent ice/water repellent coatings for solar panels.

Keywords: Optical Transmission, Reflection, Albedo, Phase Change, Surface Wettability, Attenuation, Image Analysis, Solidification

1 Introduction

1.1 Research Motivation

Advancement in technology has led to an ever-increasing demand for energy generation, with the major sources of energy being fossil fuels [1, 2]. Burning these fossil fuels has led to an increase in global carbon dioxide emissions and other hazardous air pollutants. These pollutants give rise to many ailing health conditions, subsequently reducing the quality of life [3, 4]. An increasing number of residential areas, small businesses, institutions, and industries are switching to renewable energy sources, predominantly solar energy for their daily energy needs [5].

A major challenge lies in the usage of solar PV in cold climatic conditions [6]. The buildup of fog, frost or snow occurs when the temperatures plummet, obstructing the light falling on the photo-voltaic panels. This causes a drop in the efficiency of photo-voltaic panels as much as 50% [7, 8, 9, 10]. Some studies report that partial covering of solar panels caused by ice and snow is actually more harmful than the full covering [11, 12]. To address this, various types of expensive, niche coatings have been developed including water-repellant, ice-phobic, and lubricant-infused surfaces [13, 14, 15, 16, 17, 18, 19, 20]. Application of such coatings on solar panels greatly improve water/ice phobicity but they also alter optical transmission and degrade power output. Optically transparent coatings for adverse weather conditions are scarce [21, 22]. These specialty coatings are proprietary, require specialized equipment, and are cost-prohibitive. They are out of the reach of the common man who must rely on easily available and cost-friendly products for hydrophobicity or ice-phobicity. Some of these coatings have durability issues [23, 24] which potentially can cause eventual degradation in optical transmission when they wear off. Even superhydrophobic surfaces deteriorate when exposed to continuous icing and de-icing cycles. In humid weather, the performance of superhydrophobic surfaces is reduced due to condensation between the surfaces leading to higher ice-adhesion strength [25]. Most prior studies have focused on the water/ice-repellance factor and its tunability with surface

2

coatings. However, the change in optical transmission during freezing especially when different coatings are applied has been relatively unexplored. The main focus of the current study is to develop a methodology to characterize optical transmission through water droplets as they undergo solid-liquid phase change on glass slides coated with commercially available sprays (such as RainX and HydroView).

1.2   Water-Ice Phase Change and the Effect of Surface Coatings

Many studies have been conducted in the past to understand the freezing process and the dependence of ice nucleation on the surface properties of the substrate such as wettability, surface roughness, and anti-soiling characteristics. Ice nucleation experiments have found that the freezing dynamics are dependent not only on the thermodynamic state (meteorological conditions) but also on the surrounding gases [26, 27]. Additionally, the substrate's surface roughness and the fluid properties were also found to influence ice nucleation rates on surfaces along with different wettabilities [28]. For environments having relative humidity less than 100%, it was found that hydrophobic, smooth, and thermally conductive surfaces are most efficient in delaying freezing [29]. For environments having dissolved pollutants in the atmosphere like H_2SO_4, ice nucleation from microscale water droplets required a higher saturation rate at lower temperatures [30]. Decreasing the water-surface contact area reduced the probability of ice nucleation by diminishing the surface-water heat transfer [31, 32]. Fuller et al [33] reported that the surface coatings with a higher surface roughness would lead to a much longer freezing time.

Many investigations have been conducted to understand the impact of hydrophobicity of various surfaces on water-ice solidification. An experimental study of freezing of impinging water droplets on hydrophilic and hydrophobic surfaces showed that the surface wettability had a negligible effect on the contact angle of the frozen droplet [34]. Barker et al [35] observed that both hydrophilic and hydrophobic coatings showed

3

a reduction in snow accumulation over the solar panel. No significant change in power production was observed when compared to uncoated solar panels. However, it was noted that continuous icing and de-icing cycles reduce the effectiveness of the ice-phobicity of the material by a substantial amount [36]. Cox et al [37] developed a numerical model to control the ice nucleation by tweaking the surface hydrophilicity. To understand the wettability and roughness of different surfaces, a many-body dissipative particle dynamics (MDPD) study was conducted by Du et al [38]. They found that once the surface exhibits superhydrophobicity, the surface roughness stops influencing the water-repellent property of the surface. They also reported that the contact angle changed from the Wenzel state (where water completely wets the surface) to the Cassie-Baxter State (liquid partially wets the surface, with air pockets present between the liquid and surface), on increasing the hydrophobicity on a rough surface. In summary, it is still unclear what kind of coating is needed to reduce snow accumulation while simultaneously reducing the loss of optical transmission.

1.3   Effect of Surface Coatings on Optical Transmission through Water and Ice

Water is an optically translucent medium with a higher refractive index than air. So, a sessile droplet of water will refract the light as it passes through it. This effect is used in many applications and is commonly referred to as the lensing effect of the water [39, 40]. During solid-liquid phase change, as the water droplet gradually turns into ice, its volume increases leading to a change in the overall shape of the droplet [41]. Additionally, due to the change in molecular geometry and volume, water and ice have different refractive indices causing a change in optical transmission. The ice-water interface reflects light (characterized by a reflection factor known as albedo) and consequently results in a reduction of light transmission [42, 43, 44, 45]. David and Sheng [46] and Stefan et al. [47] observed that the attenuation coefficient of water is a function of the water quality. Each body of water has a different composition, which directly affects

4

the formation of ice [48, 49, 50]. Due to this the reported values of albedo (reflection at the water-ice interface) and optical attenuation coefficient values are spread over a wide range [51]. Studying the transmission dependence on spectral wavelengths, Jerlov et al [52] and Gordon et al [53] found that short and long wavelengths (red and violet) of the visible spectrum were observed to scatter and get absorbed over a much shorter distance, while intermediary wavelengths such as green light, were found to penetrate the most. Additionally, the particles mixed in water can scatter wavelengths up to four times their diameter [54]. This has a direct effect on how different wavelengths in the spectrum interacts with water and ice [55, 56, 42, 57, 58, 59]. Another major factor that may lead to an increase in attenuation is the formation of gas bubbles. The dissolved air within water gets trapped as bubbles during the process of liquid-solid phase change [60, 61, 62].

Jaiswal et al [63] found through their investigations that although hydrophobic surfaces with high surface roughness repel ice, they do so at the cost of optical transmission. Superhydrophobic surfaces generally exhibit low optical transmission due to both the nature of the coating and the curvature of the water droplet. An increase in curvature increases reflection making the droplet appear very bright, but doesn't allow much light to pass through [64, 65]. When the anti-soiling properties of hydrophobic coatings were investigated, it was found that up to a certain period, they can keep the surfaces clean, with minimal soiling, but as time went on, due to the accumulation of insoluble particles, leading to cementation, the anti-soiling effects were drastically reduced. This lead to a substantial drop in transmittance of the coatings and to maintain the efficiency, the coatings need to be properly cleaned and reapplied every three to four weeks [66, 67, 68].

From the above discussion, it is evident that the current understanding of the change in optical properties of a water droplet undergoing liquid-solid phase change on coated substrates is lacking. There is limited data on the effectiveness of widely accessible common coatings that will likely be used by consumers to mitigate icing. The present study aims to bridge this gap by exploring if the reduction in optical transmission is

5

governed by the evolving shape of the solidifying droplet or by the phase change of water into ice. An effort is made to characterize the performance of surface coatings with different hydrophobicity from both an optical and ice-phobic perspective. The change in optical transmission through a sessile water droplet is characterized while it undergoes solidification using a Beer-Lambert Law approach originally developed by Bellur et al [69].

2   Methodology

2.1   Experimental Design

To study the shape evolution of a sessile water droplet undergoing solidification, it needs to be viewed along the horizontal direction (i.e from the side) but to study light transmission through the droplet, it needs to be viewed in the vertical direction (i.e through the droplet). Therefore, a bidirectional imaging experimental setup (Figure 1) was developed for visualization of the freezing process. The setup is divided into three parts: the optical stage, the droplet deposition stage, and the cooling stage.

Optical stage   consists of the bottom camera, the side camera, and the light source. The bottom camera is a DinoLite Premier Series Digital Microscope AM4113ZTL with 20x to 90x zoom to characterize the change in optical transmission through the droplet. The side camera is PixeLink PL-X9524 (HDR), attached to a Navitar 12x variable zoom lens. The zoom lens and the camera are connected using a c-mount extension tube. The light source (60W warm LED) is placed at the focal point of a parabolic reflector and then passed through a diffuser.

Droplet deposition stage   comprises a flat-tipped 22 gauge needle attached to a $500\,\mu L$ threaded plunger from Hamilton Company. The plunger is initially positioned over the substrate for deposition and removed right after using a retractable arm. The distance at which the droplet is deposited from the side camera is kept constant for
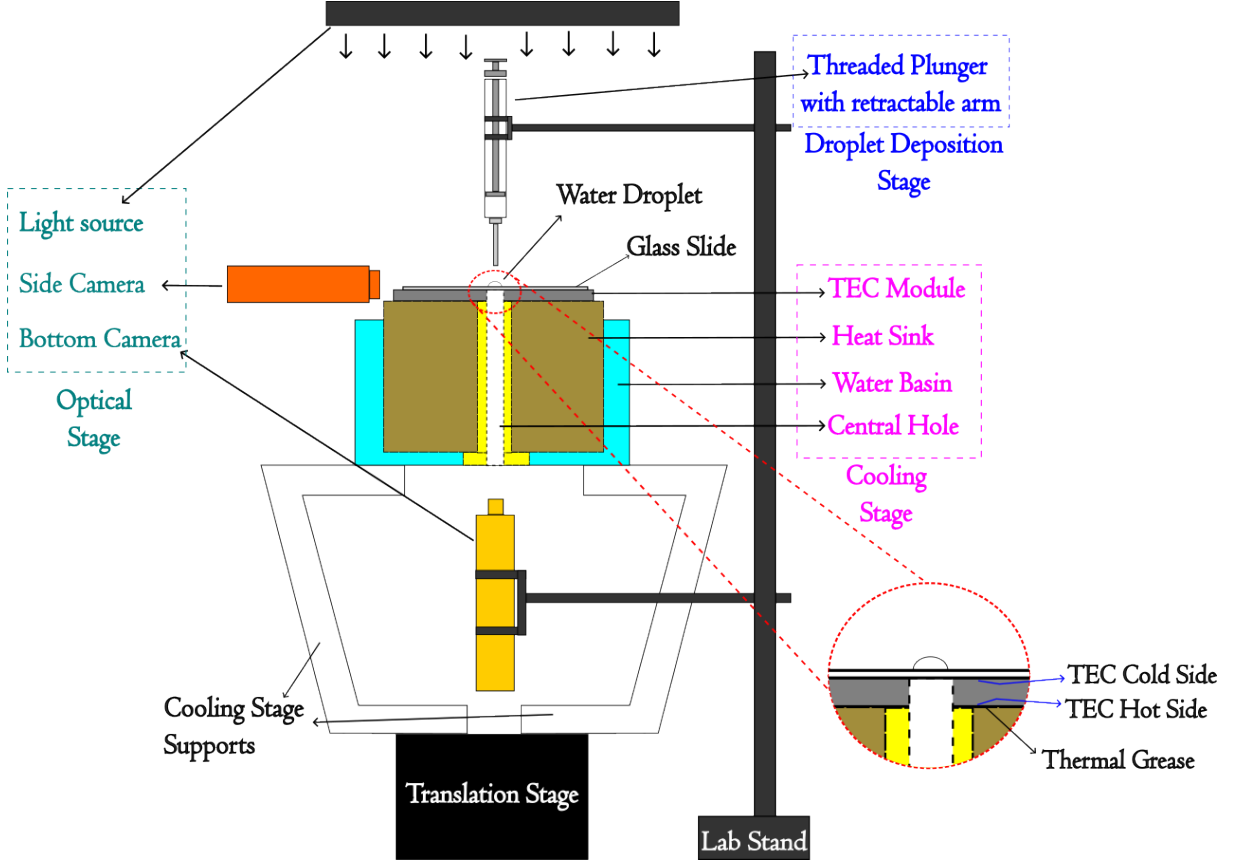
Figure 1: Schematic diagram of the experimental setup, with the optical stage, cooling stage, and the droplet deposition stage and inset figure depicting the cooling stage parts right under the droplet.

each droplet deposition. This enables simultaneous imaging from both the cameras throughout the deposition and freezing process.

Cooling stage   rests entirely on top of an XYZ translation stage. The test substrate (glass slide) rests on a TE Technology thermoelectric cooler (TEC) with a central hole, connected to a variable power supply. The cold side of the TEC module faces up, while the hot side is glued to an aluminum heatsink using thermal grease as depicted in figure 1. The heat sink rests in a water basin, which is 3D-printed using ABS and post-processed using acetone vapor smoothening. This entire setup rests upon a translation stage using 3D-printed supports. The translation stage is used to move the deposited droplet into the focus of both the cameras and helps facilitate smoother droplet deposition. The glass slide is coated with Indium Tin Oxide (ITO) on the

7

bottom. Due to its high thermal conductivity, the ITO coating enables faster/better heat transport when placed on the TEC. ITO is of particular interest because it is both conductive and optically transparent. The wettability can also be tuned depending on various treatments during the coating process [70, 71]. The ITO film was sputter-coated coating using a Denton Discovery 24. The coating thickness for the ITO is approximately 100 nm and was found to be slightly hydrophobic with a contact angle around 105 °(figure 10). The top of the glass slide was either kept bare or coated with either RainX or HydroView (commonly available hydrophobic coatings in the market for car windshields and other glasses) as per factory instructions.
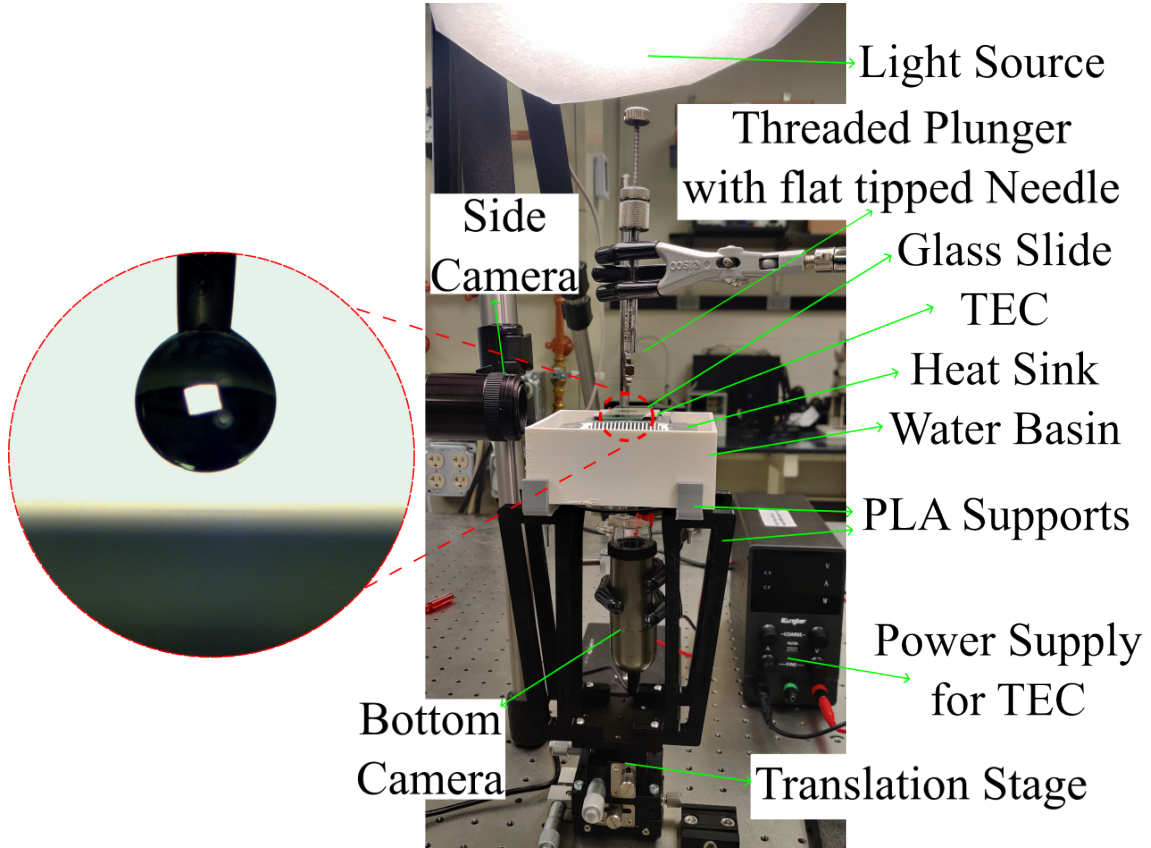

Figure 2: Experimental setup, showing the optical stage, droplet deposition stage and cooling stage with the inset figure showcasing the hanging droplet from the needle tip, over the glass slide during the droplet deposition process.

Before a test is run, the reference image from the bottom camera is taken to characterize the background light intensity of the light from the surroundings (referred to

as the background image). Then the light source is turned on and a picture of the light source is taken from the bottom camera, to quantify the intensity of the light source (referred to as the reference image).

To deposit a droplet, the threaded plunger is slightly rotated, so a hanging droplet forms at the tip of the needle. Then the glass slide is gently brought up by turning the translation stage's Z direction gauge (figure 2). The slide is brought up to the height where it gently touches the droplet. The droplet, still hanging from the tip of the needle, spreads slightly over the glass surface. Next, the glass slide is gently lowered at which point the droplet detaches from the needle and rests on the glass slide. The droplet is then brought into the focus of both cameras with minor adjustments (if needed) and thereafter the focus remains unchanged for the entire duration of the experiment. The threaded plunger is retracted from its position, so it no longer obstructs the light source. The pixel pitch is characterized using a resolution target. The frame rate for the bottom and side cameras was set at 30 frames per second.

To begin the experiment, the water basin is filled with regular tap water. Droplets of de-ionized water, of volume $2\,\mu L$ to $5\,\mu L$ were used for the experiments. The power supply is set at 20W before the droplet deposition. A droplet (at room temperature $22°C$ - $24°C$) is deposited according to the steps mentioned above. Following this, the threaded plunger is retracted, and the glass slide is lowered till the droplet comes into focus of the bottom camera by carefully turning the screw gauges of the XYZ translation stage. The entire deposition process takes approximately 15s. At this point, recording is started on both the cameras and the power to the TEC module is increased to 34W. The system's temperature is noted using a handheld FLIR IR camera E60. The coldest noted temperature on the cold side was -26°C, while the hot side was at $33°C$. At the central point on the glass slide where the droplet was deposited, the temperature was -9.8°C. The closer the temperature is to $0°C$, the longer the wait time for droplet freezing. Long wait times inevitably introduce undesirable dew formation and droplet evaporation. On the other hand, ultra-low substrate temperatures create thermal perturbations and higher spatio-temporal gradients. Setting the glass slide

temperature to -9.8°C was the best compromise to minimize the thermal perturbation without the detriments of a long freezing time. Once the droplet freezes completely, the power supply is turned off and the cameras stop recording. The glass slide is then removed and air dried. A wait time of around 15 minutes is prescribed to let the water in the basin cool down before the process can be repeated.

The cameras are set to record till the entire droplet is frozen. The duration of the freezing process is reported in Table 1. The droplet on Rainx coating almost takes seven minutes to freeze and the process of phase change from start to finish takes more than a minute. The solidification process takes longer to start on ITO compared to the uncoated glass slide, despite it being a conductive coating. This is because ITO displays slight hydrophobicity with the average contact angle being 95°. Whereas, the droplet on Hydroview, despite having a similar contact angle to ITO, displays much delayed freezing time compared to ITO, since Hydroview is non-conductive. These results show that both surface wettability and conductivity can influence ice-nucleation delay.

Coatings	Average duration for droplet solidification
No Coating	6s
RainX	72s
HydroView	12s
ITO	9s

Table 1: Reported time taken for freezing on different coatings and uncoated surface taken over 5 readings

2.2 Image Processing

The images obtained from the bottom camera are processed to study the change in optical transmission as the water freezes. The images obtained from the side camera are used to visualize the evolution of the droplet shape so that it can be coupled to the optical transmission through post-processing.

Characterization of the optical transmission is done using the Beer-Lambert Law where the intensity of the light passing through an optical medium exponentially reduces with distance d and is dependent on the material's attenuation coefficient. It is

10

modified to account for the amount of light that gets reflected from the surface of the optical medium by:

$$I = (I_0 - I_R)e^{-\mu d},$$

(1)

where I_O is the intensity of the incident light, I_R is the intensity of the light reflected from the surface of the optical medium, μ is the attenuation coefficient of the medium, d is the thickness of the medium through which the light passes, and I is the intensity of the light exiting the medium.
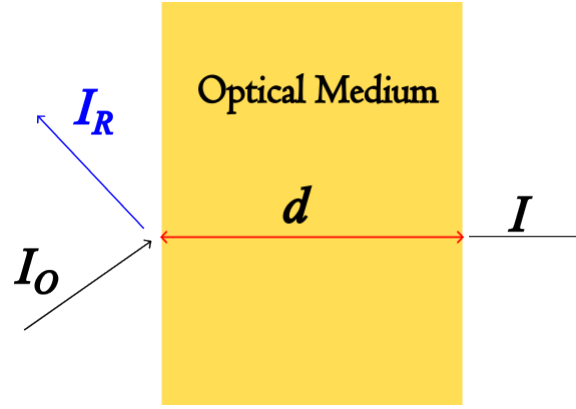

Figure 3: Optical transmission through an optical medium, where I_O is the incident intensity falling on the optical medium, I_R is the intensity of the light that gets reflected from at the surface of the optical medium, d is the thickness of the optical medium, and I is the intensity of the resultant light that exists the medium.

Transmission can be computed using two methods: (1) using the modified Beer-Lambert law which accounts for reflection, equation 1, along with the side camera droplet profile, and (2) using bottom camera images. The second method characterizes the transmission obtained experimentally and does not account for reflection.

Using the images obtained from the bottom camera, the experimentally obtained transmission ($T_{Experiment}$) can be computed [69]:

$$T_{Experiment} = \frac{I_{Test} - I_B}{I_{Reference} - I_B}$$

(2)

where I_{Test} is the bottom camera pixel intensity obtained as the droplet undergoes

freezing, $I_{Reference}$ is the pixel intensity of the reference image containing the light source without droplet and I_B is the background image without either the light source or the droplet. I_{Test} is obtained from the image frames obtained from the bottom camera as the droplet undergoes freezing, $I_{Reference}$ and I_B are obtained from the reference and background images (that were taken before the start of the experiment) respectively. The pixel intensity values from the bottom camera are extracted by performing a line scan along the diameter of the droplet and rotating it 2000 times by 0.18 degrees. Pixel intensities in these multiple-line scans are extracted and then averaged to obtain intensity along the diameter of the droplet (figure 4). The obtained average pixel intensity of the light source, $I_{Reference}$, is 240 ± 3 and the average pixel intensity for the background noise, I_B, is 7 ± 2.

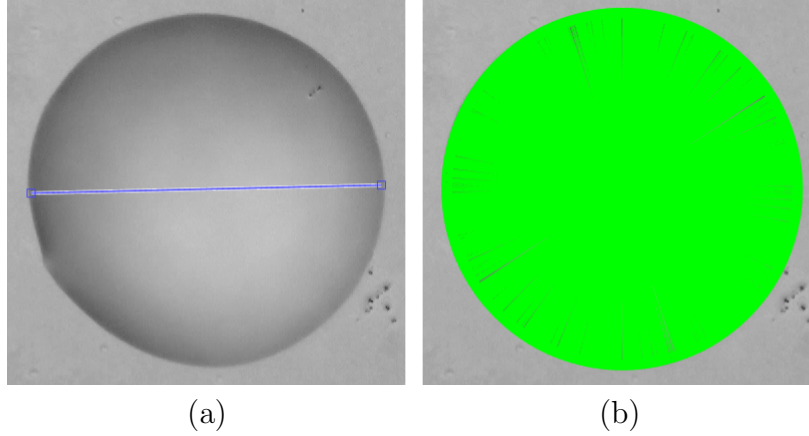(a)   (b)

Figure 4: (a) Linescan done along the diametric length of the droplet (b) 2000 rotations of the line scans, done to extract the pixel intensities, and averaged out to obtain the pixel intensity along the diametric length.

To make the comparison easier, the length of the line is normalized by the diameter of the droplets (D_N). Then the area under the transmission curve (figure 5) at each normalized instance of freezing time (t_N) of the freezing process is calculated to obtain the area-averaged transmission, T_A. The effect of the surface coatings on optical transmission is quantified by analyzing the spatiotemporally varying T_A data.

The droplet profile at different instances of freezing is extracted by first filtering the frames through a binary filter. Only the pixel intensities less than a threshold value
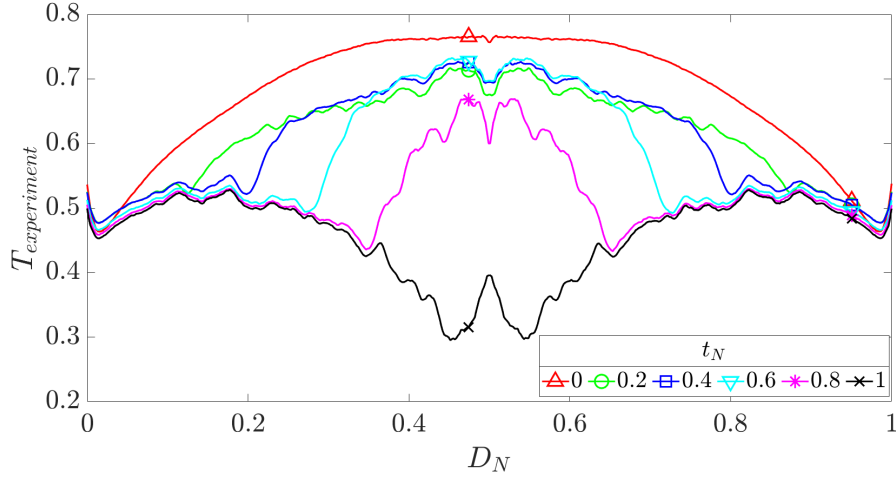
12

Figure 5: Optical transmission across the diameter of the droplet.

are recorded as 1 and the rest as 0. The filtered data is then run through a Canny edge detection algorithm and a Region of Interest (ROI) mask to obtain the droplet profile. The extracted shape profile and the original frame are then overlayed on one another, and correlated to obtain the location of the freeze front. Thus the height of the ice layer is obtained at the instantaneous freezing time. This is used to track the growth of the freeze-front as the droplet solidifies (figure 6).

The obtained height of the droplet and freeze-front location is used to calculate the theoretical transmission, $T_{Theoretical}$. This method also accounts for the intensity of the reflected light and the equation 1 is re-written as,

$$T_{Theoretical} = (1 - A_I)e^{-\mu d} \tag{3}$$

Where A_I is the albedo or the amount of reflection occurring at the interface. For Albedo = 1 all of the incident light is reflected and for a surface with Albedo = 0 all of the incident light is either transmitted through it or absorbed.

Three distinct interfaces exist as the droplet undergoes solidification, the air-water interface, the air-ice interface, and the water-ice interface (figure 6). The albedo at each interface is anticipated to be different. Using equation 3 the transmission at each medium can be computed and then added together to obtain total theoretical
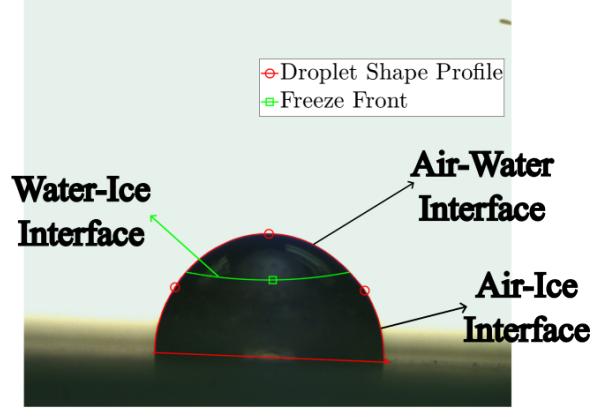
13

Figure 6: Extracted droplet shape profile and the freeze front overlayed on the original image.

transmission. Since accurate values for albedo are not available, these become tuning parameters to fit theoretical transmission from equation 3 to experimentally measured transmission.
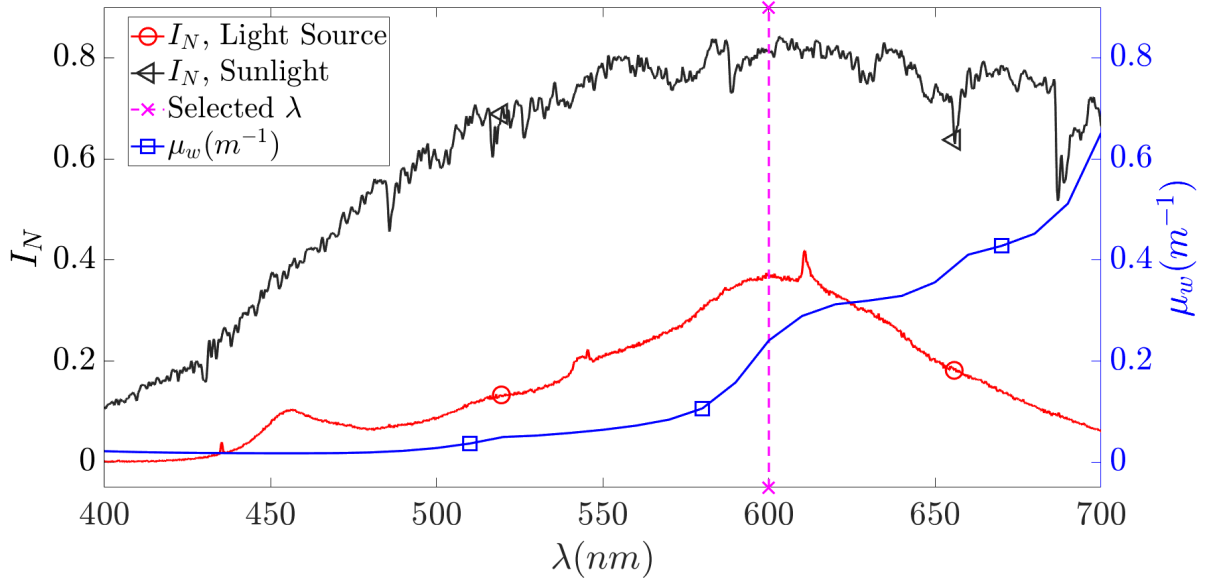

Figure 7: Wavelength dependency of the attenuation coefficient of water (μ_w) [56] plotted against spectral intensity, I_N of the light source and sunlight to determine the wavelength having the most Intensity (by area-weighted averaging) and thereby its influence on optical attenuation through water.

To account for the dependency of the optical properties of water and ice on the spectral wavelength, the wavelength of the light source is characterized using a Thorlabs

14

CCS200 spectrometer. It is observed from figure 7 that at a wavelength of $600\,\text{nm}$ emitted by the light source, the intensity is highest, which also corresponds to peak values of intensity in natural solar radiation. Therefore optical properties of water and ice are considered at $600\,\text{nm}$ and a constant attenuation coefficient, μ_w value at this wavelength is considered in the rest of this study.

3   Results

Figures 8 and 9 show images from both the bottom and side cameras for an uncoated substrate and an ITO coated substrate respectively. It is evident that: (1) the freezing leads to a reduction in optical transmission through the droplet as evidenced by the darkening of the bottom camera images and (2) the freezing process changes the drop shape as seen in the side camera images. The black spots observed in the images from the bottom view in figure 8 are air bubbles that get trapped as the water freezes to become ice. These spots are more prominent on hydrophilic substrates due to their larger surface area and consequently increased heat transfer. If the rate at which the ice layer grows is faster than the rate at which the air can diffuse, air gets trapped as bubbles. The air bubbles play a vital role in attenuating the light as it passes through the droplet. Additionally, striations are visible at the center of the freezing droplet, where water is present over the freezing front. These striations are attributed to the migration of trace gas bubbles [72] and other spontaneous surface irregularities at the evolving water-ice interface. As the droplet freezes completely, the striations disappear, suggesting that most of these striations are momentary and occur only at the freeze-front layer between water and ice. They may be the cause of scattering reflection at the water-ice interface which also has been discussed in the past by Brown et al [73].

The lensing effect of the water droplet is visible at $t_N = 0$, where the outer edges of the droplet are much darker compared to the central bright spot. And as freezing progresses, the central bright spot becomes progressively darker due to the development of trapped air bubbles. As the water droplet has the maximum height at the center,
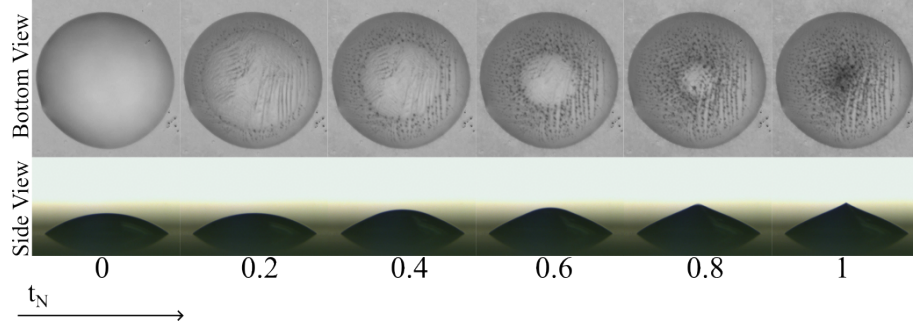
15

Figure 8: Droplet solidification imaged from the bottom and side on an uncoated substrate, shown at normalized timesteps.
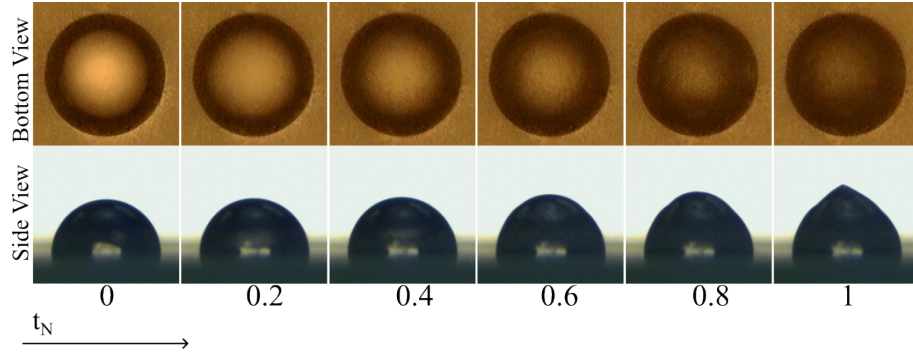

Figure 9: Droplet solidification imaged from the bottom and side on ITO-coated glass substrate, shown at normalized timesteps.

therefore it has the highest concentration of trapped air bubbles. As it is observed the cluster of the trapped air bubbles forms a dense dark spot, which leads to a sudden drop in transmission as the droplet ends up freezing, which is also noticeable in figure 8.

3.1 Contact Angle Analysis

The contact angle for the deposited droplet is calculated from the frames obtained from the side camera. The contact angle is calculated by using the Low Bond-Axisymmetric Drop Shape Analysis algorithm in ImageJ [74]. The contact angle values are averaged over 5 readings (figure 10). It is noted that all three of our coatings display hydrophobicity and RainX has the highest contact angle. It is observed that ITO coating is more hydrophobic than HydroView, which is a market-available coating meant for

regular everyday use. The uncoated glass slide shows a moderate hydrophilic nature characteristic of most clean glass surfaces, with a contact angle of 45°.
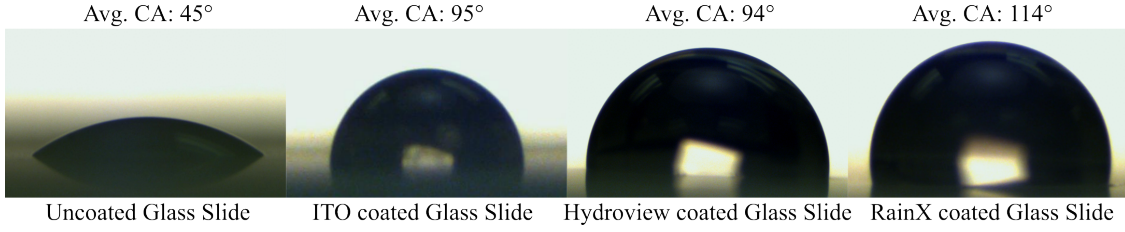

Figure 10: Deposited droplet on surfaces of different wettabilites.

The freezing process did not seem to affect the contact angle of the droplets. Since the freezing process on a hydrophobic surface takes a longer time, this leads to additional dew condensation and subsequent frost halo formation in the regions surrounding the droplet [75]. This frost halo leads to an error in contact angle measurement ($\pm 5°$) in the later stages of freezing and makes the contact line of the droplet difficult to detect. The contact angle in the later stages of freezing is obtained by estimating and matching the curvature of the droplet.

3.2   Effect of Surface Coatings

Experimental optical transmission ($T_{experimental}$) was calculated from the bottom camera images, using the method described in the image processing section. The transmission profile is integrated over the entire droplet to develop an average transmission metric (T_A). The resulting data are shown in figure 11 where t_N is the normalized freezing time for each dataset. $t_N = 0$ indicates start of freezing and $t_N = 1$ indicates end of freezing.

A general trend of decrease in transmittance behavior is observed as the droplet freezes over both coated and uncoated substrates. As soon as freezing commences, the transmittance reduces instantly but there is little to no change in shape in the earlier stages of freezing (figure 8). This behavior of the transmittance curve is inferred to be caused by the change in the material properties, as water solidifies to become ice at the base region near the substrate. At the later stage of the freezing process, the
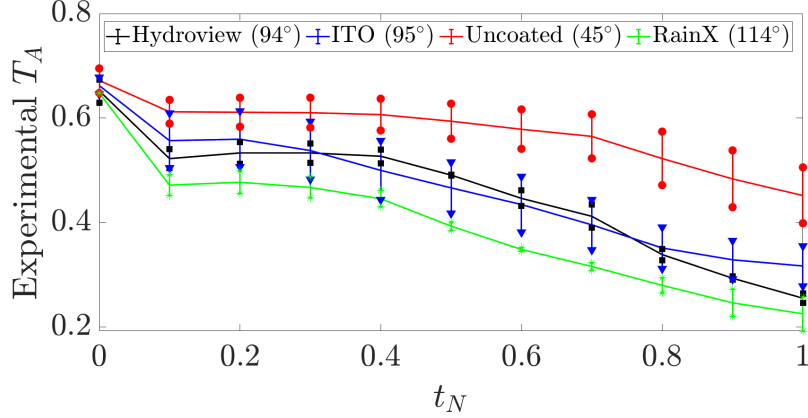
17

Figure 11: Evolution of area-averaged transmittance on different coatings as phase change occurs

change in droplet shape causes a further decrease at around $t_N = 0.7$ due to a change in reflection at the water-air interface and additional attenuation.

The uncoated glass substrates (avg. CA 45°) offer a higher transmittance than the substrates that were coated with hydrophobic coatings. The RainX coating (avg. CA 114°) has the least transmission than all the other cases studied. The bulk transmission for ITO (avg. CA 95°) and Hydroview (avg. CA 94°) coatings are very similar. In general, a decrease in overall transmission is observed as the contact angle increases. This is clear evidence that although superhydrophobic coatings may offer excellent water/ice repelling qualities but they are detrimental to optical transmission.

3.3 Freeze Front Motion

The raw pixel intensities from the bottom camera for both uncoated and ITO coated substrates are shown in figure 12 across the normalized diameter (D_N). The center of the droplet is at $D_N = 0.5$. In both cases, the intensity gradually reduces as the droplet freezes. The uncoated substrate exhibits a low contact angle where the droplet is spread over a larger area with reduced height. In this case, the transmission contribution from the change in optical properties is much larger than the attenuation contribution. As a result, it is possible to locate the freeze front as a distinct minima in the pixel in intensities (vertical dotted lines in figure 12(a)). As the droplet freezes, this freeze front

18

moves inward to the center of the drop reducing transmission due to higher albedo and attenuation of ice. In the case of a hydrophobic surface such as ITO (figure 12(b)) it is not possible to locate this freeze front from the bottom camera due to increased droplet height resulting in higher attenuation and reflection loss. The transmission is calculated using equation 3 with inputs from image data as described in section 2.2.

The lensing effect of water droplets mentioned earlier is also seen in figure 12(b) where the edges have lower pixel intensities compared to the center. At the center of the droplet, the pixel intensity reduces sharply toward the end of freezing due to the emergence of the conical tip. This reduction is due to an increase in reflection and attenuation at the ice tip.
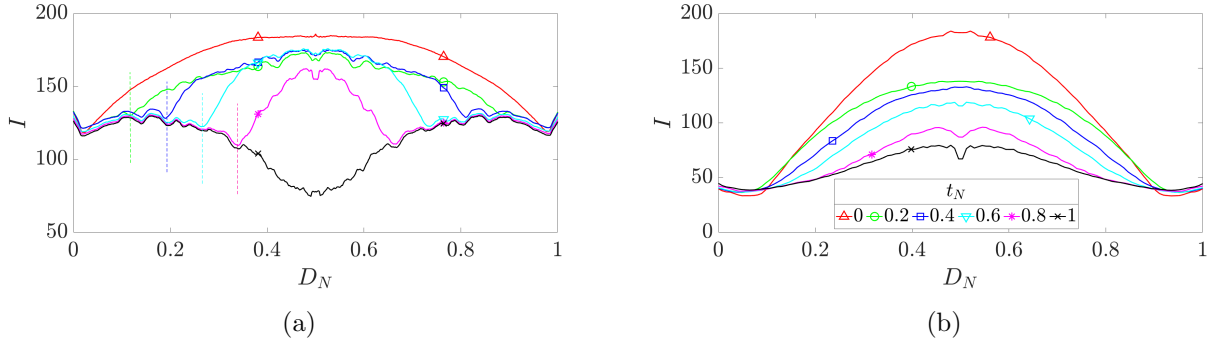

(a)

(b)

Figure 12: Change in pixel intensity through the droplet on an (a) uncoated glass slide with dashed lines pointing to the position of the freeze-front as it moves inwards and, (b) ITO Coating, shown at different instances of normalized freezing time. The vertical dotted lines in (a) show the location of the freeze front.

The images taken from the side camera to track the droplet shape evolution (figure 8) show that during the first 60-70% of freezing, the droplet shape is mostly unchanged. It is not until the freeze front moves up a substantial height that a bulge appears on top caused by the expanding volume of ice. This pushes the water higher until the entirety of the water freezes and a conical tip is formed despite of the original drop shape and the contact angle. The sharp decline in transmission towards the end of freezing in figure 12(a) is likely due to: (1) an increase in attenuation due to an increase in the path length of light, (2) an abrupt change in optical properties from water to ice and (3) change in reflection since the conical ice tip is more reflective than a water dome.

19

Coatings	A_w	$\mu_w(m^{-1})$	A_{wi}	A_i	$\mu_i(m^{-1})$
Uncoated Glass	0.19	0.15	0.22	0.4	4
RainX	0.31	0.15	0.6	0.7	4
ITO	0.24	0.15	0.26	0.7	4
Hydroview	0.27	0.15	0.35	0.7	4

Table 2: Optical properties water and ice [55, 76, 59]

Figure 13a shows droplet shape and freeze front evolution along the normalized diameter for different substrates. The shape evolution data is subsequently used to calculate the theoretical transmission using equation 3 based on optical properties shown in table 2. The albedo at the water-ice interface (A_{wi}) is not well reported in literature likely due to the existence of different forms of ice and diffuse reflections at the ice-water interface. Here A_{wi} is assumed to be a value between albedo for water (A_w) and albedo for ice (A_i) and then tuned to match experimental data. The results are depicted in figure 13b. Each row of images in figure 13 represents the complementary shape evolution and transmission for different substrates. The deviations in experimental data are likely due to the presence of air bubbles. Although degassed DI water was used, air bubbles could not be avoided completely during the rapid freezing process. It was found that due to the incredibly small droplet height, μ has a negligible effect on optical transmission and the governing parameter for the reduction in optical transmission is the reflection. Therefore only the values of albedo at the interface were varied while keeping the μ values constant (table 2).

Similar imaging results are observed for other coatings as well. One key observation is that in the first instance of the freezing process, the experimental transmission dips sharply, but the theoretical transmission does not. This is because a supercooled droplet undergoes a recalescence stage where the droplet surface crystallizes rapidly. This seemingly instantaneous event precedes the solidification process of the bulk droplet, which freezes gradually [77]. Therefore, a sudden drop in transmission is observed in the beginning characterized by phase change in a small timescale. This leads to higher surface albedo properties but is anticipated to be lower than the albedo of ice. It is likely that the reflection value is constantly changing during the initial

Figure 13: Each row of the panel represents data from substrates with different coatings. Left column (a) shows evolution of the droplet shape (solid line) with freeze front tracking (dashed line) and right column (b) compares the theoretically calculated evolution of bulk transmission to experimentally obtained bulk transmission evolution.

₃₈₃ stages of freezing but is not captured here in the theoretical model which assumes a

₃₈₄ constant value of albedo.

4   Summary and Conclusions

The present study shows that the reduction in optical transmission during freezing of water droplets smaller than the capillary length is governed by a combination of attenuation, reflection and the change in droplet geometry caused by the expansion of ice. The attenuation coefficient of ice is large compared to water but this does not solely dominate in large change in optical transmission for the size of droplets tested. This is in contrast to other studies which were done on large water bodies, where the change in phase properties governs the drop in optical transmission. The largest contribution to the drop in transmission appears to be reflection at the ice-air surface and this has not been characterized well due to the various crystalline structures of ice. The application of coatings decrease the transmission. In general, higher the contact angle, lower is the transmission but also result in a slow rate of freezing. High contact angle hydrophobic coatings are commonly used for water ice-repellancy but they must be used with caution because they are detrimental to optical transmission. Unless there is research on optically transparent hydrophobic coatings, frost management on cold weather panels will be a trade-off between ice/water repellancy and optical transmission.

A theoretical transmission model is developed based on a modified Beer-Lambert approach accounting for reflection. There is uncertainty of albedo values at the ice-water interface, likely due to the different crystalline structures of ice and diffused reflections. Here, the albedo value for the ice-water interface is assumed to be between that of pure ice and pure water and tuned to match experimental data. Good agreement is achieved for reasonable values of albedo. The model suggests that it is the reflection, rather than attenuation that dominates the transmission loss. However, this is further influenced by the change in droplet shape. The results of the current study provide invaluable insight as new optically transparent ice-phobic coatings are developed in the future.

22

References

[1] World – World Energy Balances: Overview – Analysis (2020).
    URL https://www.iea.org/reports/world-energy-balances-overview/world

[2] F. Martins, C. Felgueiras, M. Smitkova, N. Caetano, Analysis of Fossil Fuel Energy Consumption and Environmental Impacts in European Countries, Energies 12 (6) (2019) 964, number: 6 Publisher: Multidisciplinary Digital Publishing Institute. doi:10.3390/en12060964.
    URL https://www.mdpi.com/1996-1073/12/6/964

[3] F. Perera, Pollution from Fossil-Fuel Combustion is the Leading Environmental Threat to Global Pediatric Health and Equity: Solutions Exist, International Journal of Environmental Research and Public Health 15 (1) (2018) 16. doi:10.3390/ijerph15010016.
    URL https://www.ncbi.nlm.nih.gov/pmc/articles/PMC5800116/

[4] J. Lelieveld, A. Haines, R. Burnett, C. Tonne, K. Klingmüller, T. Münzel, A. Pozzer, Air pollution deaths attributable to fossil fuels: observational and modelling study, BMJ 383 (2023) e077784, publisher: British Medical Journal Publishing Group Section: Research. doi:10.1136/bmj-2023-077784.
    URL https://www.bmj.com/content/383/bmj-2023-077784

[5] F. J. M. M. Nijsse, J.-F. Mercure, N. Ameli, F. Larosa, S. Kothari, J. Rickman, P. Vercoulen, H. Pollitt, The momentum of the solar energy transition, Nature Communications 14 (1) (2023) 6542, number: 1 Publisher: Nature Publishing Group. doi:10.1038/s41467-023-41971-7.
    URL https://www.nature.com/articles/s41467-023-41971-7

[6] E. Andenæs, B. P. Jelle, K. Ramlo, T. Kolås, J. Selj, S. E. Foss, The influence of snow and ice coverage on the energy generation from photovoltaic solar cells, Solar Energy 159 (2018) 318–328. doi:10.1016/j.solener.2017.10.078.

URL https://www.sciencedirect.com/science/article/pii/ S0038092X17309581

[7] R. Carriveau, A. Edrisy, P. Cadieux, R. Mailloux, Ice adhesion issues in renewable energy infrastructure, Journal of Adhesion Science and Technology 26 (4-5) (2012) 447–461. doi:10.1163/016942411X574592.

[8] F. Cucchiella, I. D'Adamo, Estimation of the energetic and environmental impacts of a roof-mounted building-integrated photovoltaic systems, Renewable and Sustainable Energy Reviews 16 (7) (2012) 5245–5259. doi:10.1016/j.rser.2012.04.034.
URL https://www.sciencedirect.com/science/article/pii/ S1364032112003097

[9] S. Senthil, K. R. Ravi, A Brief Review on Self-cleaning Coatings for Photovoltaic Systems, in: H. Tyagi, P. R. Chakraborty, S. Powar, A. K. Agarwal (Eds.), New Research Directions in Solar Energy Technologies, Springer, Singapore, 2021, pp. 197–234. doi:10.1007/978-981-16-0594-9_7.
URL https://doi.org/10.1007/978-981-16-0594-9_7

[10] R. W. Andrews, A. Pollard, J. M. Pearce, A new method to determine the effects of hydrodynamic surface coatings on the snow shedding effectiveness of solar photovoltaic modules, Solar Energy Materials and Solar Cells 113 (2013) 71–78. doi:10.1016/j.solmat.2013.01.032.
URL https://www.sciencedirect.com/science/article/pii/ S0927024813000470

[11] A. Woyte, J. Nijs, R. Belmans, Partial shadowing of photovoltaic arrays with different system configurations: literature review and field test results, Solar Energy 74 (3) (2003) 217–233. doi:10.1016/S0038-092X(03)00155-5.
URL https://www.sciencedirect.com/science/article/pii/ S0038092X03001555

24

[12] R. Andrews, A. Pollard, J. Pearce, The Effects of Snowfall on Solar Photovoltaic Performance, Solar Energy 92 (2013) 84–97. `doi:10.1016/j.solener.2013.02.014`.

[13] S. Hatte, R. Pitchumani, Novel nonwetting solid-infused surfaces for superior fouling mitigation, Journal of Colloid and Interface Science 627 (2022) 308–319. `doi:10.1016/j.jcis.2022.06.155`.
URL `https://www.sciencedirect.com/science/article/pii/S0021979722011456`

[14] S. Hatte, R. Pitchumani, Analysis of convection heat transfer on multiscale rough superhydrophobic and liquid infused surfaces, Chemical Engineering Journal 424 (2021) 130256. `doi:10.1016/j.cej.2021.130256`.
URL `https://www.sciencedirect.com/science/article/pii/S1385894721018441`

[15] L. Mishchenko, B. Hatton, V. Bahadur, J. Taylor, T. Krupenkin, J. Aizenberg, Design of ice-free nanostructured surfaces based on repulsion of impacting water droplets, ACS Nano 4 (12) (2010) 7699–7707. `doi:10.1021/nn102557p`.

[16] S.-H. Lee, M. Seong, M. Kwak, H. Ko, M. Kang, H. Park, S. Kang, H. Jeong, Tunable Multimodal Drop Bouncing Dynamics and Anti-Icing Performance of a Magnetically Responsive Hair Array, ACS Nano 12 (11) (2018) 10693–10702. `doi:10.1021/acsnano.8b05109`.

[17] R. Stoddard, K. Nithyanandam, R. Pitchumani, Steam condensation heat transfer on lubricant-infused surfaces, iScience 24 (4) (2021) 102336. `doi:10.1016/j.isci.2021.102336`.
URL `https://www.sciencedirect.com/science/article/pii/S2589004221003047`

[18] R. Stoddard, K. Nithyanandam, R. Pitchumani, Fabrication and durability characterization of superhydrophobic and lubricant-infused surfaces, Journal of Colloid and Interface Science 608 (2022) 662–672. `doi:10.1016/j.jcis.2021.09.099`.

25

URL   https://www.sciencedirect.com/science/article/pii/
S0021979721015587

[19] M. Kreder, J. Alvarenga, P. Kim, J. Aizenberg, Design of anti-icing surfaces: Smooth, textured or slippery?, Nature Reviews Materials 1 (1) (2016). `doi:` `10.1038/natrevmats.2015.3.`

[20] K. Kant, R. Pitchumani, Fractal textured glass surface for enhanced performance and self-cleaning characteristics of photovoltaic panels, Energy Conversion and Management 270 (2022) 116240. `doi:10.1016/j.enconman.2022.116240.`
URL   https://www.sciencedirect.com/science/article/pii/
S0196890422010172

[21] S. Sutha, S. Suresh, B. Raj, K. R. Ravi, Transparent alumina based superhydrophobic self–cleaning coatings for solar cell cover glass applications, Solar Energy Materials and Solar Cells 165 (2017) 128–137. `doi:10.1016/j.solmat.2017.02.027.`
URL   https://www.sciencedirect.com/science/article/pii/
S0927024817300892

[22] J. Y. Hee, L. V. Kumar, A. J. Danner, H. Yang, C. S. Bhatia, The Effect of Dust on Transmission and Self-cleaning Property of Solar Panels, Energy Procedia 15 (2012) 421–427. `doi:10.1016/j.egypro.2012.02.051.`
URL   https://www.sciencedirect.com/science/article/pii/
S1876610212003876

[23] C. M. da Silva, P. Rodrigues Muniz, Evaluation of Low-Cost Hydrophobic Coatings in the Performance of Photovoltaic Modules, in: 2021 14th IEEE International Conference on Industry Applications (INDUSCON), 2021, pp. 746–752. `doi:10.1109/INDUSCON51756.2021.9529744.`
URL https://ieeexplore.ieee.org/abstract/document/9529744

[24] K. Isbilir, B. Maniscalco, R. Gottschalg, J. M. Walls, Test Methods for Hydrophobic Coatings on Solar Cover Glass, in: 2017 IEEE 44th Photovoltaic Specialist

Conference (PVSC), 2017, pp. 2827–2832. `doi:10.1109/PVSC.2017.8366246`.

URL `https://ieeexplore.ieee.org/abstract/document/8366246`

[25] S. A. Kulinich, S. Farhadi, K. Nose, X. W. Du, Superhydrophobic Surfaces: Are They Really Ice-Repellent?, Langmuir 27 (1) (2011) 25–29. `doi:10.1021/la104277q`.

URL `https://pubs.acs.org/doi/10.1021/la104277q`

[26] M. A. Holden, J. M. Campbell, F. C. Meldrum, B. J. Murray, H. K. Christenson, Active sites for ice nucleation differ depending on nucleation mode, Proceedings of the National Academy of Sciences 118 (18) (2021) e2022859118. `doi:10.1073/pnas.2022859118`.

URL `https://pnas.org/doi/full/10.1073/pnas.2022859118`

[27] S. Jung, M. K. Tiwari, N. V. Doan, D. Poulikakos, Mechanism of supercooled droplet freezing on surfaces, Nature Communications 3 (1) (2012) 615. `doi:10.1038/ncomms1630`.

URL `https://www.nature.com/articles/ncomms1630`

[28] K. Li, S. Xu, W. Shi, M. He, H. Li, S. Li, X. Zhou, J. Wang, Y. Song, Investigating the Effects of Solid Surfaces on Ice Nucleation, Langmuir 28 (29) (2012) 10749–10754. `doi:10.1021/la3014915`.

URL `https://pubs.acs.org/doi/10.1021/la3014915`

[29] F. Montes Ruiz-Cabello, S. Bermúdez-Romero, P. F. Ibáñez-Ibáñez, M. Cabrerizo-Vílchez, M. Rodríguez-Valverde, Freezing delay of sessile drops: Probing the impact of contact angle, surface roughness and thermal conductivity, Applied Surface Science 537 (2021) 147964. `doi:10.1016/j.apsusc.2020.147964`.

URL `https://linkinghub.elsevier.com/retrieve/pii/S0169433220327215`

[30] T. Koop, H. P. Ng, L. T. Molina, M. J. Molina, A New Optical Technique to Study Aerosol Phase Transitions: The Nucleation of Ice from H_2SO_4 Aerosols, The Journal of Physical Chemistry A 102 (45) (1998) 8924–8931. `doi:10.1021/`

27

jp9828078.

URL https://pubs.acs.org/doi/10.1021/jp9828078

[31] A. Alizadeh, M. Yamada, R. Li, W. Shang, S. Otta, S. Zhong, L. Ge, A. Dhino-jwala, K. R. Conway, V. Bahadur, A. J. Vinciquerra, B. Stephens, M. L. Blohm, Dynamics of Ice Nucleation on Water Repellent Surfaces, Langmuir 28 (6) (2012) 3180–3186. doi:10.1021/la2045256.

URL https://pubs.acs.org/doi/10.1021/la2045256

[32] T. Inada, H. Tomita, T. Koyama, Ice nucleation in water droplets on glass surfaces: From micro- to macro-scale, International Journal of Refrigeration 40 (2014) 294–301. doi:10.1016/j.ijrefrig.2013.11.024.

URL https://linkinghub.elsevier.com/retrieve/pii/S0140700713003654

[33] A. Fuller, K. Kant, R. Pitchumani, Analysis of freezing of a sessile water droplet on surfaces over a range of wettability, Journal of Colloid and Interface Science 653 (2024) 960–970. doi:10.1016/j.jcis.2023.09.119.

URL https://www.sciencedirect.com/science/article/pii/S0021979723018179

[34] Z. Zhu, X. Zhang, Y. Zhao, X. Huang, C. Yang, Freezing character-istics of deposited water droplets on hydrophilic and hydrophobic cold surfaces, International Journal of Thermal Sciences 171 (2022) 107241. doi:10.1016/j.ijthermalsci.2021.107241.

URL https://www.sciencedirect.com/science/article/pii/S1290072921004026

[35] A. J. Barker, T. A. Douglas, E. M. Alberts, P. A. IreshFernando, G. W. George, J. B. Maakestad, L. C. Moores, S. P. Saari, Influence of chemical coatings on solar panel performance and snow accumulation, Cold Regions Science and Technology 201 (2022) 103598. doi:10.1016/j.coldregions.2022.103598.

URL https://linkinghub.elsevier.com/retrieve/pii/S0165232X22001173

[36] Y. Wang, J. Xue, Q. Wang, Q. Chen, J. Ding, Verification of Icephobic/Anti-icing Properties of a Superhydrophobic Surface, ACS Applied Materials & Interfaces 5 (8) (2013) 3370–3381, publisher: American Chemical Society. `doi:10.1021/am400429q`.
URL `https://doi.org/10.1021/am400429q`

[37] S. J. Cox, S. M. Kathmann, B. Slater, A. Michaelides, Molecular simulations of heterogeneous ice nucleation. I. Controlling ice nucleation through surface hydrophilicity, The Journal of Chemical Physics 142 (18) (2015) 184704. `doi:10.1063/1.4919714`.
URL `https://pubs.aip.org/jcp/article/142/18/184704/193816/Molecular-simulations-of-heterogeneous-ice`

[38] Q. Du, P. Zhou, Y. Pan, X. Qu, L. Liu, H. Yu, J. Hou, Influence of hydrophobicity and roughness on the wetting and flow resistance of water droplets on solid surface: A many-body dissipative particle dynamics study, Chemical Engineering Science 249 (2022) 117327. `doi:10.1016/j.ces.2021.117327`.
URL `https://linkinghub.elsevier.com/retrieve/pii/S0009250921008927`

[39] F. Chowdhury, K. Chau, Microscopy using water droplets, Proceedings of SPIE - The International Society for Optical Engineering 8252 (2012) 31. `doi:10.1117/12.906949`.

[40] S. Buddies, The Magnifying Effect of a Water Drop (Jul. 2015).
URL `https://www.scientificamerican.com/article/the-magnifying-effect-of-a-water-drop/`

[41] C. Zhang, H. Zhang, W. Fang, Z. Yugang, C. Yang, Axisymmetric lattice Boltzmann model for simulating the freezing process of a sessile water droplet with volume change, Physical Review E 101 (Feb. 2020). `doi:10.1103/PhysRevE.101.023314`.

[42] C. McKay, G. Clow, D. Andersen, Wharton, Light transmission and reflection in perennially ice-covered Lake Hoare, Antarctica, J. Geophys. Res. 99 (Nov. 1994).

604   doi:10.1029/94JC01414.

[43] D. K. Perovich, Light reflection from sea ice during the onset of melt,
     Journal of Geophysical Research: Oceans 99 (C2) (1994) 3351–3359,
     _eprint: https://onlinelibrary.wiley.com/doi/pdf/10.1029/93JC03397. doi:10.
     1029/93JC03397.
     URL https://onlinelibrary.wiley.com/doi/abs/10.1029/93JC03397

[44] D. H. Dolan, Y. M. Gupta, Nanosecond freezing of water under multiple shock
     wave compression: Optical transmission and imaging measurements, The Journal
     of Chemical Physics 121 (18) (2004) 9050–9057. doi:10.1063/1.1805499.
     URL   https://pubs.aip.org/jcp/article/121/18/9050/535332/
     Nanosecond-freezing-of-water-under-multiple-shock

[45] C. Katlein, S. Arndt, M. Nicolaus, D. K. Perovich, M. V. Jakuba, S. Suman,
     S. Elliott, L. L. Whitcomb, C. J. McFarland, R. Gerdes, A. Boetius, C. R.
     German, Influence of ice thickness and surface properties on light transmis-
     sion through A rctic sea
     ice, Journal of Geophysical Research: Oceans 120 (9) (2015) 5932–5944.
     doi:10.1002/2015JC010914.
     URL   https://agupubs.onlinelibrary.wiley.com/doi/10.1002/
     2015JC010914

[46] D. Christian, Y. P. Sheng, Relative influence of various water quality parameters
     on light attenuation in Indian River Lagoon, Estuarine, Coastal and Shelf Science
     57 (5) (2003) 961–971. doi:10.1016/S0272-7714(03)00002-7.
     URL   https://www.sciencedirect.com/science/article/pii/
     S0272771403000027

[47] H. Stefan, J. Cardoni, F. Schiebe, C. Cooper, Model of Light Penetration in a
     Turbid Lake, WATER RESOURCES RESEARCH 19 (1) (1983) 109–120, num
     Pages: 12 Place: Washington Publisher: Amer Geophysical Union Web of Science
     ID: WOS:A1983QR71000013. doi:10.1029/WR019i001p00109.

URL https://www.webofscience.com/api/gateway?GWVersion=2&SrcAuth=
DOISource&SrcApp=WOS&KeyAID=10.1029%2FWR019i001p00109&DestApp=DOI&
SrcAppSID=USW2EC0EF6IRLpUMBYMnGfDZzu9O5&SrcJTitle=WATER+RESOURCES+
RESEARCH&DestDOIRegistrantName=American+Geophysical+Union

[48] X. Ye, E. Anderson, P. Chu, C. Huang, P. Xue, Impact of Water Mixing and Ice Formation on the Warming of Lake Superior: A Model-guided Mechanism Study, Limnology and Oceanography 64 (2019) 558–574. doi:10.1002/lno.11059.

[49] Z. Lei, B. Chen, S. D. Brooks, Effect of Acidity on Ice Nucleation by Inorganic–Organic Mixed Droplets, ACS Earth & Space Chemistry 7 (12) (2023) 2562–2573. doi:10.1021/acsearthspacechem.3c00242.
URL https://www.ncbi.nlm.nih.gov/pmc/articles/PMC10749479/

[50] M. Berton, E. Nathan, H. R. Ghazizadeh Karani, T. Girona, C. Huber, P. Williard, J. Head, Experimental Investigations on the Effects of Dissolved Gases on the Freezing Dynamics of Ocean Worlds, Journal of Geophysical Research: Planets 125 (Aug. 2020). doi:10.1029/2020JE006528.

[51] S. G. Warren, Optical properties of ice and snow, Philosophical Transactions of the Royal Society A: Mathematical, Physical and Engineering Sciences 377 (2146) (2019) 20180161. doi:10.1098/rsta.2018.0161.
URL https://royalsocietypublishing.org/doi/10.1098/rsta.2018.0161

[52] N. Jerlov, Optical Oceanography, Elsevier, 1968, google-Books-ID: k9EjXyVJH0UC.

[53] H. R. Gordon, W. R. McCluney, Estimation of the Depth of Sunlight Penetration in the Sea for Remote Sensing, Applied Optics 14 (2) (1975) 413–416, publisher: Optica Publishing Group. doi:10.1364/AO.14.000413.
URL https://opg.optica.org/ao/abstract.cfm?uri=ao-14-2-413

[54] D. S. ENSOR, M. J. PILAT, The Effect of Particle Size Distribution on Light Transmittance Measurement, American Industrial Hygiene Association Journal 32 (5) (1971) 287–292, publisher: Taylor & Francis _eprint:

https://doi.org/10.1080/0002889718506462. `doi:10.1080/0002889718506462`.

URL `https://doi.org/10.1080/0002889718506462`

[55] J.-P. Zhao, T. Li, D. Barber, J.-P. Ren, M. Pucko, S.-J. Li, X. Li, Attenuation of lateral propagating light in sea ice measured with an artificial lamp in winter Arctic, Cold Regions Science and Technology 61 (1) (2010) 6–12. `doi:10.1016/j.coldregions.2009.12.006`.

URL `https://linkinghub.elsevier.com/retrieve/pii/S0165232X10000030`

[56] D. K. Perovich, The Optical Properties of Sea Ice, Monograph 96-1, COLD RE-GIONS RESEARCH & ENGINEERING LABORATORY (May 1996).

[57] C. Varotsos, I. Melnikova, A. Cracknell, C. Tzanis, A. Vasilyev, New spectral functions of the near-ground albedo derived from aircraft diffraction spectrometer observations, Atmospheric Chemistry and Physics 14 (Jul. 2014). `doi:10.5194/acp-14-6953-2014`.

[58] K. B. Katsaros, L. A. McMurdie, R. J. Lind, J. E. DeVault, Albedo of a water surface, spectral variation, effects of atmospheric transmittance, sun angle and wind speed, Journal of Geophysical Research: Oceans 90 (C4) (1985) 7313–7321, _eprint: https://onlinelibrary.wiley.com/doi/pdf/10.1029/JC090iC04p07313. `doi:10.1029/JC090iC04p07313`.

URL `https://onlinelibrary.wiley.com/doi/abs/10.1029/JC090iC04p07313`

[59] M. G. Cooper, L. C. Smith, A. K. Rennermalm, M. Tedesco, R. Muthyala, S. Z. Leidman, S. E. Moustafa, J. V. Fayne, Spectral attenuation coefficients from measurements of light transmission in bare ice on the Greenland Ice Sheet, The Cryosphere 15 (4) (2021) 1931–1953, publisher: Copernicus GmbH. `doi:10.5194/tc-15-1931-2021`.

URL `https://tc.copernicus.org/articles/15/1931/2021/`

[60] W. A. Murray, R. List, Freezing of Water Drops, Journal of Glaciology 11 (63) (1972) 415–429. `doi:10.3189/S0022143000022371`.

32

URL https://www.cambridge.org/core/product/identifier/ S0022143000022371/type/journal_article

[61] F. Chu, X. Zhang, S. Li, H. Jin, J. Zhang, X. Wu, D. Wen, Bubble formation in freezing droplets, Physical Review Fluids 4 (7) (2019) 071601, publisher: American Physical Society. doi:10.1103/PhysRevFluids.4.071601.
URL https://link.aps.org/doi/10.1103/PhysRevFluids.4.071601

[62] K. Shao, M. Song, J. Shen, X. Zhang, L. Pekař, Experimental study on the distribution and growth characteristics of trapped air bubbles in ice slices at different freezing temperatures, Applied Thermal Engineering 244 (2024) 122600. doi:10.1016/j.applthermaleng.2024.122600.
URL https://www.sciencedirect.com/science/article/pii/ S1359431124002680

[63] J. Jaiswal, Singh, M. Ramesh Chandra, A. Sanger, A. Kumar, S. Mourya, S. Chauhan, R. Daipuriya, Enhanced Optical Absorbance Of Hydrophobic Ti Thin Film: Role Of Surface Roughness, Advanced Materials Letters 7 (6) (2016) 485–490, publisher: International Association of Advanced Materials. doi:10.5185/amlett.2016.6056.
URL https://aml.iaamonline.org/article_14871.html

[64] L. Whitehead, M. Mossman, A. R. Kushnir, Observations of Total Internal Reflection at a Natural Super-Hydrophobic Surface, Physics in Canada - La Physique au Canada 64 (2008) 7–11.

[65] K. Isakov, C. Kauppinen, S. Franssila, H. Lipsanen, Superhydrophobic Antireflection Coating on Glass Using Grass-like Alumina and Fluoropolymer, ACS Applied Materials & Interfaces 12 (44) (2020) 49957–49962. doi:10.1021/acsami. 0c12465.
URL https://pubs.acs.org/doi/10.1021/acsami.0c12465

[66] K. K. Ilse, J. Rabanal, L. Schonleber, M. Z. Khan, V. Naumann, C. Hagendorf, J. Bagdahn, Comparing Indoor and Outdoor Soiling Experiments for Dif-

33

ferent Glass Coatings and Microstructural Analysis of Particle Caking Processes, IEEE Journal of Photovoltaics 8 (1) (2018) 203–209. `doi:10.1109/JPHOTOV.2017.2775439`.

URL `https://ieeexplore.ieee.org/document/8170288/`

[67] G. C. Oehler, F. Lisco, F. Bukhari, S. Uličná, B. Strauss, K. L. Barth, J. M. Walls, Testing the Durability of Anti-Soiling Coatings for Solar Cover Glass by Outdoor Exposure in Denmark, Energies 13 (2) (2020) 299. `doi:10.3390/en13020299`.

URL `https://www.mdpi.com/1996-1073/13/2/299`

[68] M. B. Esfahani, A. Eshaghi, S. R. Bakhshi, Transparent hydrophobic, self-cleaning, anti-icing and anti-dust nano-structured silica based thin film on cover glass solar cell, Journal of Non-Crystalline Solids 583 (2022) 121479. `doi:10.1016/j.jnoncrysol.2022.121479`.

URL `https://linkinghub.elsevier.com/retrieve/pii/S0022309322000886`

[69] K. Bellur, E. Médici, M. Kulshreshtha, V. Konduru, D. Tyrewala, A. Tamila-rasan, J. McQuillen, J. Leão, D. Hussey, D. Jacobson, J. Scherschligt, J. Hermanson, C. Choi, J. Allen, A new experiment for investigating evaporation and condensation of cryogenic propellants, Cryogenics 74 (2016) 131–137. `doi:10.1016/j.cryogenics.2015.10.016`.

URL `https://linkinghub.elsevier.com/retrieve/pii/S0011227515001423`

[70] J. Gwamuri, A. Vora, J. Mayandi, D. O. Guney, P. L. Bergstrom, J. M. Pearce, A new method of preparing highly conductive ultra-thin indium tin oxide for plasmonic-enhanced thin film solar photovoltaic devices, Solar Energy Materials and Solar Cells 149 (2016) 250–257. `doi:10.1016/j.solmat.2016.01.028`.

URL `https://linkinghub.elsevier.com/retrieve/pii/S0927024816000416`

[71] L. Hao, X. Diao, H. Xu, B. Gu, T. Wang, Thickness dependence of structural, electrical and optical properties of indium tin oxide (ITO) films deposited on PET substrates, Applied Surface Science 254 (11) (2008) 3504–3508. `doi:10.1016/j.`

742   `apsusc.2007.11.063.`

743   URL `https://linkinghub.elsevier.com/retrieve/pii/S016943320701673X`

744   [72] I. N. Pavlov, B. S. Rinkevichyus, A. V. Tolkachev, Visualization of crystallization

745   processes in the near-wall layer of a water drop, Measurement Techniques 56 (3)

746   (2013) 271–274. `doi:10.1007/s11018-013-0193-2.`

747   URL `https://doi.org/10.1007/s11018-013-0193-2`

748   [73] R. A. Brown, J. Keizer, U. Steiger, Y. Yeh, Enhanced light scattering at the ice-

749   water interface during freezing, The Journal of Physical Chemistry 87 (21) (1983)

750   4135–4138, publisher: American Chemical Society. `doi:10.1021/j100244a030.`

751   URL `https://doi.org/10.1021/j100244a030`

752   [74] A. F. Stalder, T. Melchior, M. Müller, D. Sage, T. Blu, M. Unser, Low-bond

753   axisymmetric drop shape analysis for surface tension and contact angle measure-

754   ments of sessile drops, Colloids and Surfaces A: Physicochemical and Engineering

755   Aspects 364 (1-3) (2010) 72–81. `doi:10.1016/j.colsurfa.2010.04.040.`

756   URL `https://linkinghub.elsevier.com/retrieve/pii/S0927775710002761`

757   [75] S. Jung, M. K. Tiwari, D. Poulikakos, Frost halos from supercooled water droplets,

758   Proceedings of the National Academy of Sciences 109 (40) (2012) 16073–16078,

759   publisher: Proceedings of the National Academy of Sciences. `doi:10.1073/pnas.`

760   `1206121109.`

761   URL `https://www.pnas.org/doi/full/10.1073/pnas.1206121109`

762   [76] D. K. Perovich, others, The optical properties of sea ice (1996).

763   [77] F. Tavakoli, A. Sarkissians, P. Kavehpour, When water freezes before it solidifies,

764   arXiv: Fluid Dynamics (2012).

765   URL `https://api.semanticscholar.org/CorpusID:118838335`

5   Acknowledgements

6   Appendix

Table 3: List of Symbols and Notations

Notation	Physical Quantity
I	Resultant Pixel Intensity
I_O	Incidental Intensity
μ	Attenuation Coefficient of an Optical Medium (m^{-1})
d	Thickness of an Optical medium
T	Transmittance
t_N	Normalized Time
CA	Contact Angle $(°)$
μ_w	Optical attenuation Coefficient of Water (m^{-1})
A_{wi}	Albedo at Water-Ice Interface
A_w	Albedo of Water
A_i	Albedo of Ice
μ_i	Optical attenuation Coefficient of Ice (m^{-1})
I_N	Normalized Intensity
λ	Wavelength (nm)
T_A	Area under Transmission curve or the Bulk Transmission
D_N	Normalized Diameteric Length